Applied Thermal Engineering 30 (2010) 1863–1871

Contents lists available at ScienceDirect

Applied Thermal Engineering

journal homepage: www.elsevier.com/locate/apthermeng

Investigation of bubble effect in microfluidic fuel cells by a simplified microfluidic reactor

Jin-Cherng Shyu [a,*], Chung-Sheng Wei [b], Ching-Jiun Lee [c], Chi-Chuan Wang [d]

[a] Department of Mechanical Engineering, National Kaohsiung University of Applied Sciences, Kaohsiung 80778, Taiwan
[b] Nanya Technology Corporation, Taoyuan 33859, Taiwan
[c] Institute of Applied Mechanics, National Taiwan University, Taipei 10617, Taiwan
[d] Department of Mechanical Engineering, National Chiao Tung University, Hsinchu 30010, Taiwan

ARTICLE INFO

Article history:
Received 16 November 2009
Accepted 23 April 2010
Available online 4 May 2010

Keywords:
Microfluidic
Solubility
Gas/liquid two-phase flow
Fuel cell

ABSTRACT

This study experimentally examines the influence of two-phase flow on the fluid flow in membraneless microfluidic fuel cells. The gas production rate from such fuel cell is firstly estimated via corresponding electrochemical equations and stoichiometry from the published measured current–voltage curves in the literature to identify the existence of gas bubble. It is observed that O_2 bubble is likely to be generated in Hasegawa's experiment when the current density exceeds 30 mA cm^{-2} and 3 mA cm^{-2} for volumetric flow rates of 100 μL min^{-1} and 10 μL min^{-1}, respectively. Besides, CO_2 bubble is also likely to be presented in the Jayashree's experiment at a current density above 110 mA cm^{-2} at their operating volumetric liquid flow rate, 0.3 mL min^{-1}. Secondly, a 1000-μm-width and 50-μm-depth platinum-deposited microfluidic reactor is fabricated and tested to estimate the gas bubble effect on the mixing in the similar microchannel at different volumetric flow rates. Analysis of the mixing along with the flow visualization confirm that the membraneless fuel cell should be free from any bubble, since the mixing index of the two inlet streams with bubble generation is almost five times higher than that without any bubble at the downstream.

1. Introduction

In recent years, much attention has been focused on fuel cells because of their attractive advantages, such as higher efficiency of energy conversion and no carbon dioxide emission, over the conventional combustion of gasoline and other fossil fuels. Among all kinds of current fuel cells being studied, polymer electrolyte membrane (PEM) fuel cell employing perfluorosulfonic acid polymer membranes, such as Nafion®, yields the best performance for stationary and transportation applications. As a consequence, researches associated with the PEM fuel cells development had been well elaborated.

Despite the cited promising features, the PEM has certain intrinsic problems, such as tearing, deterioration, and inefficient prevention of fuel crossover as stated by Savadogo [1]. Besides, decreasing the membrane thickness results in higher ionic conductivity but is susceptible to the fuel crossover. Moreover, in order to avoid the dehydration of the PEM for a better performance, PEM fuel cell systems like that proposed by Nguyen and White [2], Ferng et al. [3], and Williams et al. [4] as well as Wang et al. [5] are rather complex for incorporating both an external humidification system and a heat exchanger, leading to some concerns in well managing a PEMFC system.

With the advance of microfabrication technology, it has become possible to fabricate a novel microfluidic fuel cell operated without a PEM by transporting the aqueous fuel, oxidant and/or electrolyte streams in a single microchannel through different inlets under laminar flow condition. In recent years, the so-called microfluidic membraneless fuel cell has been proposed and tested by several research groups such as Ferrigno et al. [6], Choban et al. [7–9], Cohen et al. [10,11], Jayashree et al. [12], Hasegawa et al. [13], and Sun et al. [14]. Various designs of some published researches pertaining to membraneless microfluidic fuel cell are summarized in Table 1 and Fig. 1. With this smart design, both fuel crossover and water management could be avoided due to the nature of laminar liquid flow. Furthermore, adjustments of flow rates and channel dimensions allow more precise control of the electrochemical processes that are taken place at the catalyst-covered electrodes. Such microfluidic fuel cells are considered as a feasible micropower sources for miniature and portable devices. These portable devices include not only cell phones and laptop computers, but also clinical and diagnostic tests, microanalytical systems for field tests, and global positioning systems [7].

* Corresponding author. Tel.: +886 7 3814526x5343; fax: +886 7 3831373.
E-mail address: jcshyu1207@hotmail.com (J.-C. Shyu).

1359-4311/$ – see front matter © 2010 Elsevier Ltd. All rights reserved.
doi:10.1016/j.applthermaleng.2010.04.029

Table 1
Summary of various design parameters for some published membraneless microfluidic fuel cell researches.

Authors	Aqueous reactant		Catalyst/position		Catalyst deposition	Channel size (mm)	Flow rate (mL/min)
	Fuel	Oxidant	Anode	Cathode			
Choban et al. [7]	HCOOH	$KMnO_4$ O_2/H_2SO_4	Pt-black	Pt-black Opposite sidewalls	Electrodeposition	$W \times H = 0.5 \times 0.5$ $W \times H = 1.0 \times 1.0$ $L = 30$ mm	0.3–0.8
Cohen et al. [11]	H_2/KOH H_2/H_2SO_4	O_2/H_2SO_4 O_2/KOH	Pt	Pt Opposite sidewalls	E-beam evaporation	$W \times H = 1.0 \times 0.25$ $W \times H = 1.0 \times 0.38$ $L = 50$ mm	0. 5–2.0
Choban et al. [9]	CH_3OH CH_3OH/H_2SO_4	O_2/H_2SO_4	Pt/Ru Pt + Ru Pt-black	Pt-black Opposite sidewalls	Apply the catalyst suspension on the electrode and dry it	$W \times H = 0.75 \times 1.0$ $L = 29$ mm	0.15–0.4
Hasegawa et al. [13]	H_2O_2/NaOH	H_2O_2/H_2SO_4	Pt	Pt The same surface	Argon ion sputter	$W \times H = 1.0 \times 0.05$	1.44
Cohen et al. [10]	$HCOOH/H_2SO_4$	O_2/H_2SO_4	Pt	Pt Opposite sidewalls	E-beam evaporation	$W \times H = 1.0 \times 0.25$ $W \times H = 1.0 \times 0.38$ $L = 50$ mm 0.5	0.5
Choban et al. [8]	CH_3OH/H_2SO_4 CH_3OH/KOH	O_2/H_2SO_4 O_2/KOH	Pt/Ru	Pt-black Opposite sidewalls	Dry the catalyst suspension applied on the electrode	$W \times H = 0.75 \times 1.0$ $L = 29$ mm	0.3

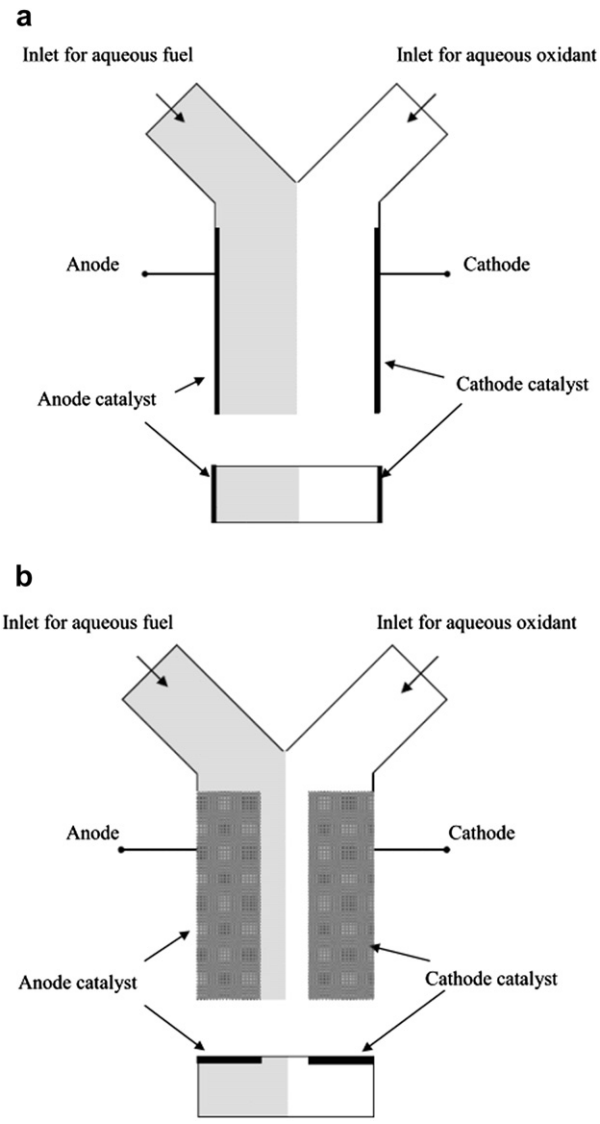

Fig. 1. Two typical designs of published membraneless microfluidic fuel cell with two inlets: (a) anode catalyst and cathode catalyst are on the opposite sidewalls, (b) both anode catalyst and cathode catalyst are on the same surface.

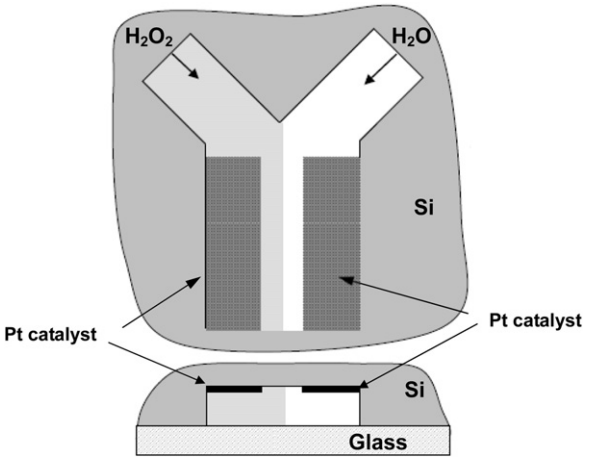

Fig. 2. Schematic illustration of the present Y-shaped microfluidic reactor design, whose catalyst is used to catalyze the H_2O_2 decomposition to imitate the bubble generation at one electrode of the membraneless microfluidic fuel cell.

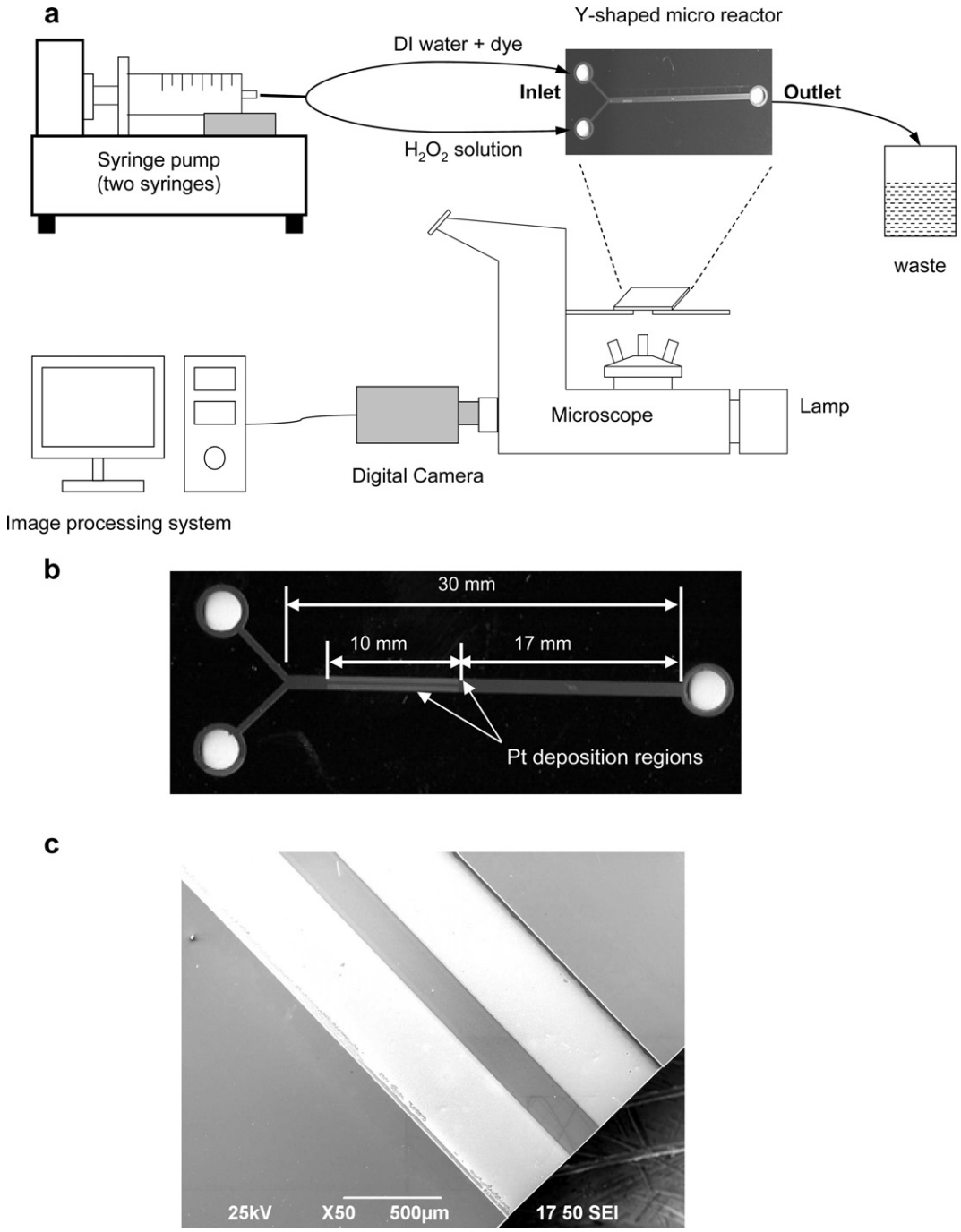

Fig. 3. (a) Schematic illustration of the present experimental system, (b) Y-shaped microfluidic reactor, (c) SEM showing the 0.2-mm-apart Pt catalysts in the microfluidic reactor.

Although such microfluidic fuel cells have numerous advantages as abovementioned, some challenges as mentioned by Kjeang et al. [15] must be overcome to realize such fuel cell in practical applications. Among them, low energy output per system volume or mass of current microfluidic fuel cells is the major shortcoming. In order to lessen the influence of its shortcoming, searching for new fuel and oxidant combination and increasing fuel utilization are regarded as effective solutions. Moreover, exploitation of independently multiple stack unit cells has also been proven to be feasible as reported in the literature [6,10,11]. However, volumetric power density of such devices would be limited due to the sealing volume and structural elements separating the cells [15].

By a careful examination of the recent researches on such membraneless microfluidic fuel cell, depending on the selection of the aqueous reactants, one would observe that gaseous product would usually be produced on one of the electrodes in the electrochemical reaction. Choban et al. [7] performed a membraneless microfluidic fuel cell experiment employing a Y-shaped microchannel with a square cross-section of either 0.5 mm × 0.5 mm or 1.0 mm × 1.0 mm. The formic acid was chosen as fuel fed at flow rates ranging from 0.1 to 0.8 mL min^{-1}. The authors mentioned that the presence of carbon dioxide bubbles would hinder the performance of the membraneless fuel cell considerably. However, they declared that carbon dioxide bubbles were never observed in their

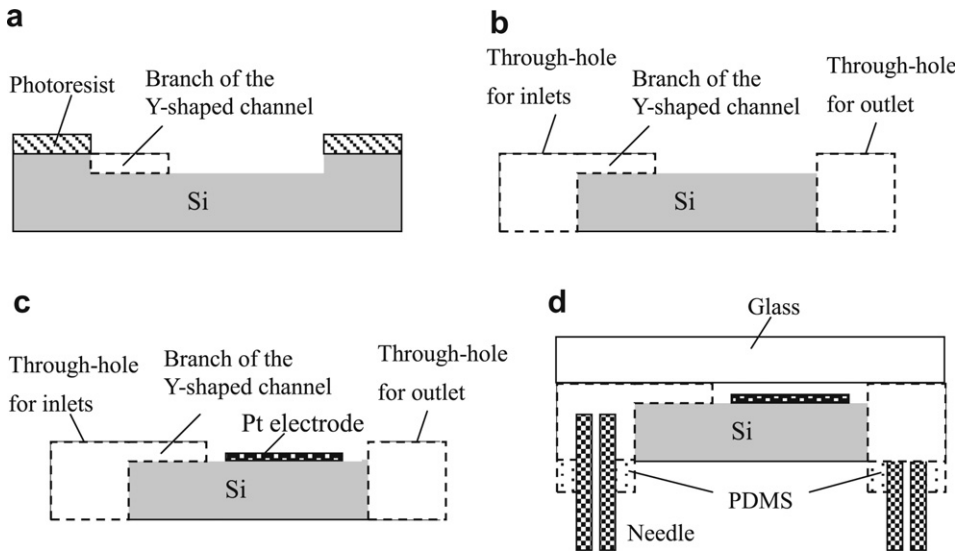

Fig. 4. The schematic illustration of the fabrication process of the microfluidic reactor in this study: (a) Etch silicon wafer by ICP-RIE to form microchannel; (b) Back side etching to form through-holes; (c) E-beam evaporation for Pt deposition; (d) Seal the inlets and outlet with PDMS after anodic bonding.

experiments due to the high solubility of CO_2 in water at room temperature. Similar statement was also made by Sun et al. [14]. They also employed formic acid as fuel catalyzed by platinum electrodes in a microchannel with 500 μm in width and 50 μm in depth.

In addition to carbon dioxide being generated from the oxidation of formic acid and methanol, other kinds of gaseous product might also be produced during the operation of membraneless microfluidic fuel cells with different aqueous reactants. Hasegawa et al. [13] proposed a novel membraneless microfuel cell using the hydrogen peroxide in alkaline/acid bipolar electrolyte as both fuel and oxidant catalyzed by platinum electrodes that were separately deposited on the channel undersurface in a Y-shaped microchannel. According to the electrochemical reaction described in their study, the electron-losing reaction at the anode is

$$\begin{aligned} &H_2O_2 + OH^- \rightarrow HO_2 + H_2O \\ &HO_2^- + OH^- \rightarrow O_2 + H_2O + 2e^- \end{aligned} \quad (1)$$

Besides, the electron-gaining reaction at the cathode is

$$H_2O_2 + 2H^+ + 2e^- \rightarrow 2H_2O \quad (2)$$

The overall electrochemical reaction is

$$2H_2O_2 + 2H^+ + 2OH^- \rightarrow 4H_2O + O_2 \quad (3)$$

Besides water and salt, oxygen is also being produced at the anode. However, there is only one figure showing the corresponding performance at different H_2O_2 concentrations subjected to a particularly huge flow rate of 24 μL s^{-1}, operated in an extremely flat microchannel, and no further discussion on the effect of oxygen on its performance was made.

It is worth noting that the solubility of oxygen in water is much less than that of carbon dioxide. In this regard, the flow characteristics may become unpredictable and uncontrollable with the presence of oxygen bubble. Accordingly, it would be interesting to examine related parameters affecting the performance of such membraneless microfluidic fuel cells. This information is especially

Table 2
Experimental conditions of the present study.

Depth of the microchannel	50 μm
Width of the microchannel	1000 μm
Length of the microchannel	30 mm
Catalyst dimension	0.4 mm × 10 mm
Inlet flow rates (μL/min)	1, 10, 100, 1000
Corresponding Re No.	0.06, 0.63, 6.35, 63.49
Liquids used	18.3 Ω cm Millipore water Hydrogen peroxide
H_2O_2 concentration	0.1 M, 1.0 M
Gaseous product	Oxygen Density: 1.43 × 10^{-3} g cm^{-3}

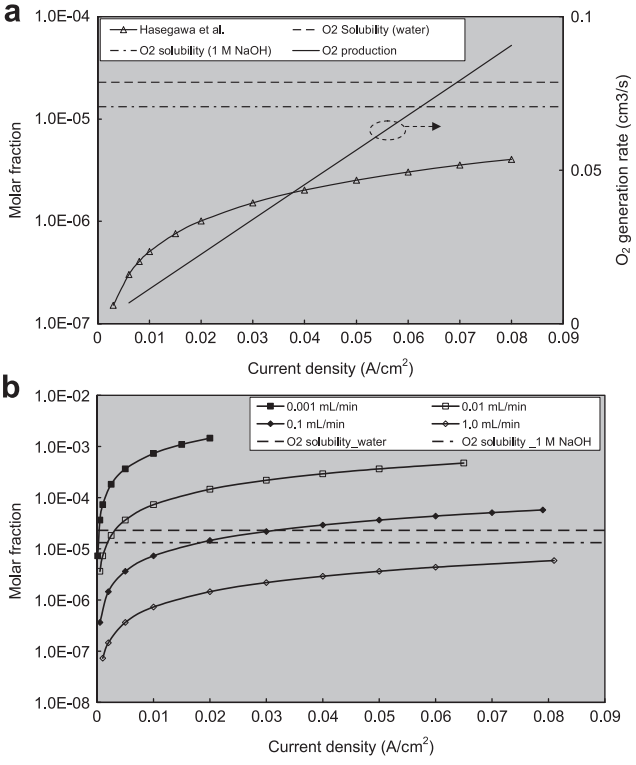

Fig. 5. Comparison of analysis results of oxygen molar fraction with oxygen solubility in water or NaOH of 1 M in the Y-shaped microchannel at different current density; (a) Hasegawa case and calculated oxygen production rate, (b) different liquid volumetric flow rate ranged from 0.001 to 1 mL min^{-1}.

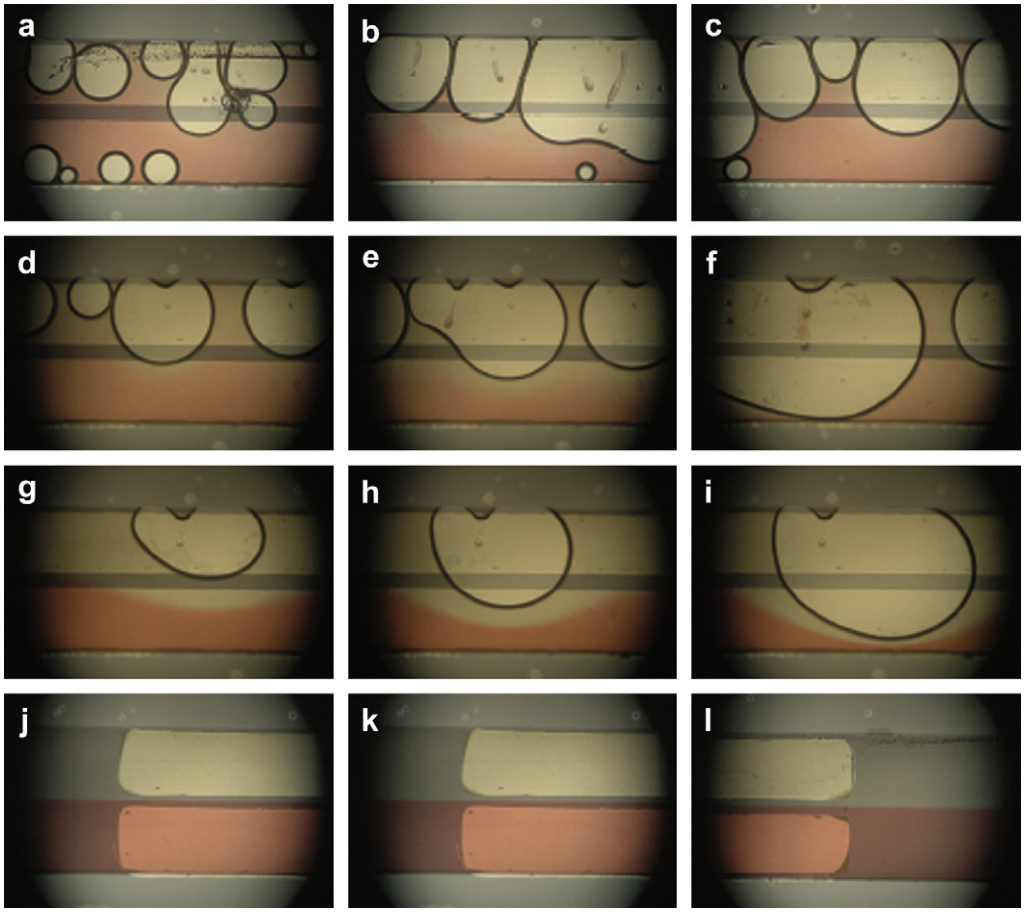

Fig. 6. Both H_2O_2 of 0.1 M and water with red dye were driven into the Y-shaped microfluidic reactor for flow visualization, volumetric flow rate for cases: (a)–(c) is 1 μL min^{-1}; (d)–(f) is 10 μL min^{-1}; (g)–(i) is 100 μL min^{-1}; (j)–(l) is 1000 μL min^{-1}.

vital for numerical simulation without taking into consideration of the influence of two-phase flow as performed by Bazylak et al. [16] and Chen et al. [17] since it may mislead the physical insight provided the oxygen bubbles is being generated in the microchannel.

Therefore, the objective of the present study is to clarify the influence of bubble flow on the fluid flow in membraneless microfluidic fuel cells based on the published results. This is made by firstly predicting the bubble being engendered from the electric generation process of the membraneless microfluidic fuel cell published in the literature using a theoretical analysis based on stoichiometry and the solubility of the gaseous product at the operating condition. Secondly, in order to realize the oxygen bubbles effect on such fuel cell performance, flow visualization is performed for a platinum-deposited Y-shaped microfluidic reactor as shown in Fig. 2. The dimension is the same as that of Hasegawa et al. [13]. Oxygen is produced due to the decomposition of hydrogen peroxide catalyzed by platinum to simulate the similar flow conditions of the aforementioned microfluidic fuel cell proposed by Hasegawa et al. [13]. Based on the flow visualization results, effect of the generated bubble on the performance of such membraneless microfluidic fuel cell will also be discussed.

2. Experimental apparatus

A schematic of the present flow field visualization is shown in Fig. 3, it consists of three major components, including a microfluidic reactor with a Y-shaped microchannel, a fluid delivery system and an image recording and acquisition system.

A single sided polished silicon wafer having a thickness of 500 μm was used to fabricate the microfluidic reactor with a Y-shaped microchannel. The fabrication process shown in Fig. 4 contains three photolithography and etched steps, as well as the anodic bonding, for the wafer to achieve the essential features of the microfluidic reactor.

In order to form a 50-μm-depth and 1000-μm-width Y-shaped microchannel by ICP-RIE (Inductively Coupled Plasma Reactive Ion Etching, MESC Multiplex ICP, Surface Technology Systems) etching, the first photolithography step was conducted with photoresist AZ-P4620 by a conventional i-line aligner. Subsequently, a lithography process followed by the other ICP etching was carried out on the backside of the wafer to introduce three 3-mm-diameter through holes as the fluid inlets and outlet, as shown in Fig. 4(b). The final lithography step incorporates platinum catalyst by lift-off process on the bottom surface of the Y-shaped microchannel. This was achieved by employing E-beam evaporation to deposit a layer of platinum adhered to a titanium layer on silicon wafer after patterning the photoresist (AZ-P4620) on the wafer, as shown in Fig. 4(c). The photoresist for all lithography processes in the forgoing processes was removed by soak in acetone followed by DI water rinse. Note that the platinum catalyst was deposited on either one single side or two sides of the microchannel in length and width of 10 mm and 0.4 mm, respectively.

After the fabrication processes of the Y-shaped microfluidic reactor for a silicon wafer, anodic bonding of the wafer with a 500 μm thick Pyrex 7740 glass wafer was carried out to seal the microchannel. The assembly was then diced to produce individual

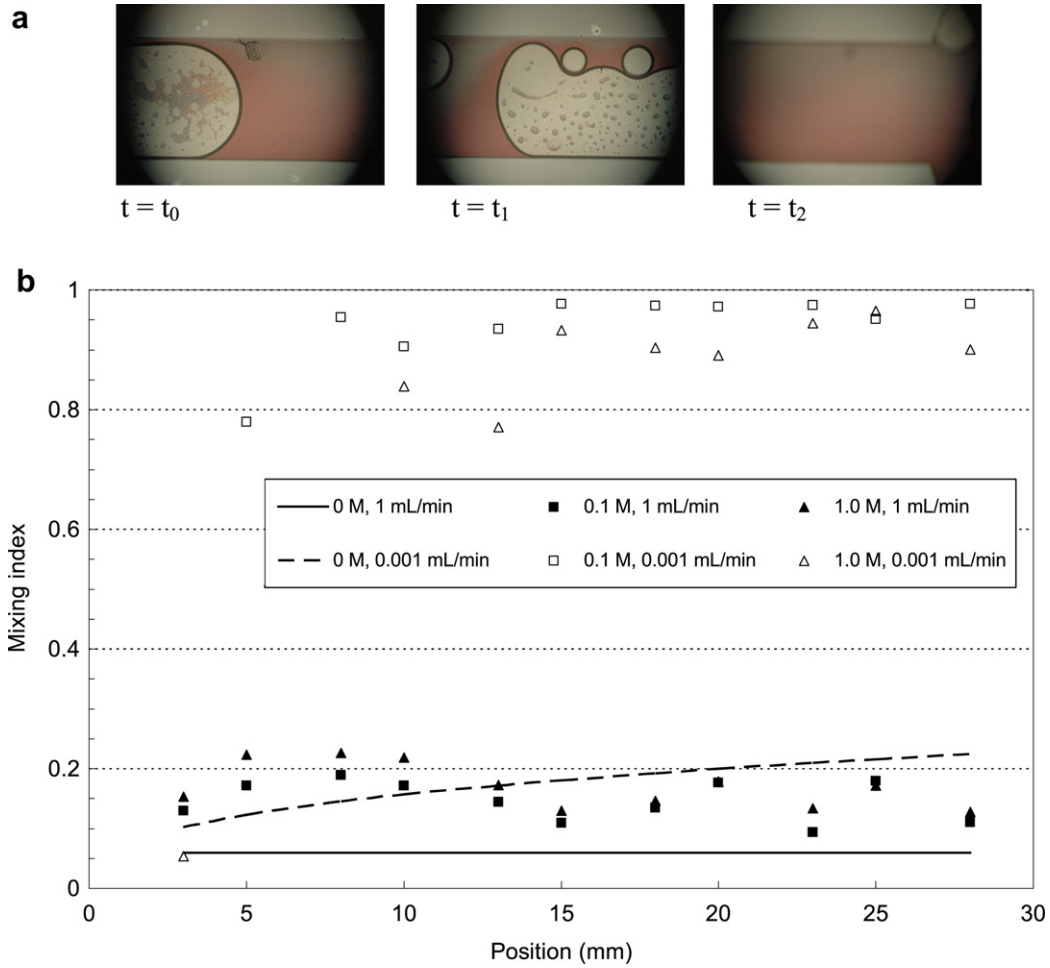

Fig. 7. (a) The downstream concentration distribution and bubble characteristics for case of $[H_2O_2] = 0.1$ M and water with red dye with volumetric flow rate of 1 μL min^{-1}, $t_0 < t_1 < t_2$; (b) the mixing between two streams in the present microfluidic reactor with $[H_2O_2] = 0$, 0.1 M and 1 M at volumetric flow rates of 0.001 mL min^{-1} and 1 mL min^{-1}.

chip. Each through hole was sealed by PDMS, as shown in Fig. 4(d). The working fluids can flow in and out through the needles connected to the fluid delivery system.

For the fluid delivery system, a syringe pump (KDS 210, KD Scientific Inc.) with two syringes was employed. Polyethylene tubing is used to deliver liquid into the Y-shaped microchannel and to guide the waste stream out of the channel. Both 18.3 MΩ-cm Millipore water and hydrogen peroxide with concentrations of 0.1 M or 1 M were simultaneously pumped into the Y-shaped microchannel via individual inlet having the same volumetric flow rate. During the experiment, we also conduct flow visualization using red dye (new coccine) injection into the Y-shaped microchannel. The experimental conditions are summarized in Table 2.

The image recording and acquisition system comprises an inverted optical microscope with a 10× object lens, a digital camera (Nikon D70) with 3008(H) × 2000(V) pixels, a quartz halogen illuminator (Dolan-Jenner Industries, 170D), and a personal computer for image acquisition.

For further examining the bubble effect on the concentration distribution of the two streams, all pictures were analyzed for mixing index estimation in the following equation [18]:

$$M_I = 1 - \sqrt{\frac{1}{N}\sum\left(\frac{I(j) - \bar{I}}{\bar{I}}\right)^2} \tag{4}$$

where N is the number of total pixels, I denotes the intensity of each pixel, and $\bar{I}$ is the mean intensity value of all pixels.

3. Results and discussion

According to the electrochemical reaction described in Eq. (1) and stoichiometry, a transfer of two mole electrons accompanies the production of one mole oxygen in the alkaline electrolyte, and the oxygen generation rate could be exactly estimated at different current densities for the fuel cell proposed by Hasegawa et al. [13] as shown in Fig. 5(a) based on the given active electrode area and the cross-sectional area of the microchannel, namely 0.026 cm^2 and 1 mm × 0.05 mm, respectively. Meanwhile, one could also calculate the molar fraction of oxygen (X_g) and the oxygen production rate (Q_g) at various current densities in the microchannel per unit time interval based on the given volumetric flow rate of the aqueous reactants as shown in Fig. 5(a).

$$Q_g = \frac{C_d A}{2F}\ (\text{mol/s}) = \frac{C_d A}{2F}\frac{M_g}{\rho_g}\left(\text{cm}^3/\text{s}\right) \tag{5}$$

$$X_g = \frac{\frac{Q_g \rho_g}{M_g}}{\frac{Q_l \rho_l}{M_l} + \frac{Q_g \rho_g}{M_g}} \tag{6}$$

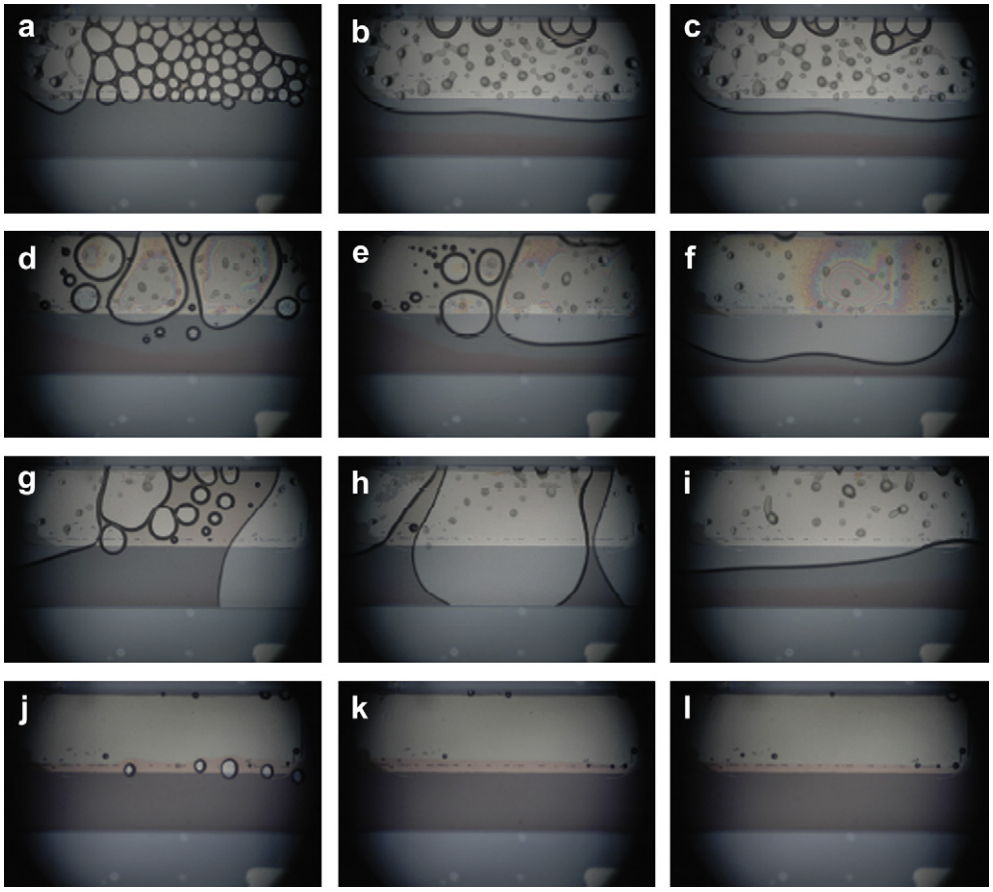

Fig. 8. Both H_2O_2 of 1.0 M and water with red dye were driven into the Y-shaped microfluidic reactor for flow visualization, volumetric flow rate for cases: (a)–(c) is 1 μL min^{-1}; (d)–(f) is 10 μL min^{-1}; (g)–(i) is 100 μL min^{-1}; (j)–(l) is 1000 μL min^{-1}.

where Q, C_d, A, F, M, ρ are volumetric flow rate, current density, active electrode area, Faraday constant, molecular weight, and density, respectively. Besides, the subscripts g and l denote the gas and liquid. Note that the volumetric flow rate in all figures of this study represents the inlet volumetric flow of one single stream, and the total volumetric flow rate in microchannel is twice of the value. It is an identical expression with all published data cited below.

From the aforementioned analyzed result, one could observe that oxygen bubble is unlikely to form with a current generation being less than 80 mA cm^{-2}, since the molar fraction of oxygen produced in that fuel cell is less than its solubility in water or in the alkaline electrolyte ([NaOH] = 1 M) obtained from handbook [19]. This is due to a particularly huge amount of supplied volumetric flow rate (24 μL s^{-1}).

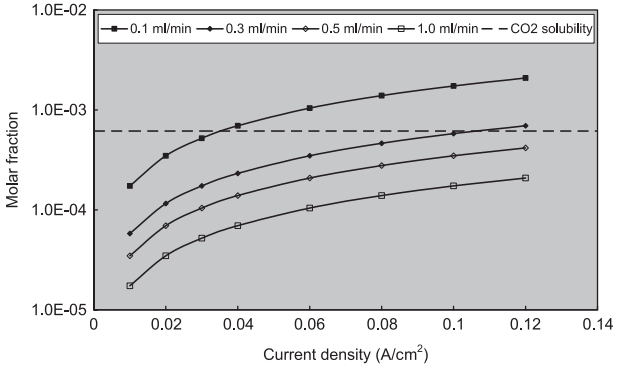

Fig. 9. Comparison of analysis results of CO_2 molar fraction with CO_2 solubility in water in the membraneless microfluidic fuel cell proposed by Jayashree et al. [12] with volumetric liquid flow rate ranged from 0.1 to 1.0 mL min^{-1}.

In fact, as can be seen from Fig. 5(b), oxygen bubbles will be generated provided oxygen molar fraction produced in the memebraneless microfluidic fuel cell is higher than the solubility of oxygen in water or in 1 M NaOH solution (horizontal dashed line) at a specific current density. Therefore, oxygen bubbles would be generated in the microchannel when the current density exceeds 30 mA cm^{-2} and 3 mA cm^{-2} for volumetric flow rates of 100 μL min^{-1} and 10 μL min^{-1}, respectively. Besides, when operated at a larger volumetric flow rate, bubble generation entails a higher threshold current density as shown in Fig. 5(b). According to the results shown in Fig. 5, it is found that with the larger volumetric flow rate, lesser oxygen molar fraction is produced at a given current density. In addition, more oxygen could be produced with the increase of current density at a given volumetric flow rate. The results implicate that gas bubbles in such microfluidic fuel cell would be easier to be formed either at the condition of higher current production or at a lower volumetric flow rate of the reactant.

For further clarification of the influence of the gas/liquid two-phase flow effect on the flow field of such membraneless microfluidic fuel cell, flow visualization is then carried out for a Y-shaped microfluidic reactor in accordance with the same dimension of Hasegawa et al. [13]. In such microfluidic reactor, oxygen is produced on one of the catalyst in contact with H_2O_2 solution through the catalytic decomposition of hydrogen peroxide as follows:

$$2H_2O_2 \rightarrow 2H_2O + O_2 \quad (7)$$

Photos that represent hydrogen peroxide and water with injection of red dye in the Y-shaped microfluidic reactor at 0.1 M subjected to various volumetric flow rates are shown in Fig. 6, where (a)–(c) is 1 μL min^{-1}; (d)–(f) is 10 μL min^{-1}; (g)–(i) is 100 μL min^{-1}; and (j)–(l) is 1000 μL min^{-1}. As is clearly shown in the figure, bubble is generated when the volumetric flow rate is less or equal to 100 μL min^{-1}. A calculation of the corresponding gas superficial velocity and liquid superficial velocity suggests the two-phase flow patterns fall with the slug/bubbly region of the corresponding microchannel based on the flow pattern proposed by Kawaji and Chung [20]. Note that in microchannel, the size of the detached bubble is comparable or much larger than the microchannels, this is especially applicable when the system pressure is low or moderate like present case. In this regard, the bubble/slug being generated can easily fill up the channel, significantly altering the interface of the two streams, or even mixing up the two streams completely as shown in Fig. 7(a). In either case, it would doom the performance of fuel cell due to less effective electrode area or crossover phenomenon. Actually, compared to the case without any addition of H_2O_2, denoted as 0 M, the mixing index estimated by Eq. (4) of the two inlet streams due to the effect of bubble generation in the microchannel is almost fivefold as compared to that at the downstream shown in Fig. 7(b) with a lower volumetric flow rate, 0.001 mL min^{-1}.

In addition, the periodic generation and detachment of the bubble/slug flow pattern result in intermittent flow field along the microchannel, which eventually lead to an unstable fuel cell operation. This can be made clear from the progress of flow pattern (e.g. Fig. 6(a)–(c), (d)–(f) or (g)–(i)) where the generated small bubbles agglomerated with each other to become larger slug/plug, yet the detachment of larger slug give way to liquid refilling. The cyclic intermittent process caused by the slug flow inevitably offset the performance of required laminar flow. In the meantime, the two-phase flow pattern is no longer in existence when the volumetric flow rate is raised to 1000 μL min^{-1}. This again agrees with the foregoing discussion that no bubble will be observed provided that it is within the solubility threshold. Analogous observation prevails for a concentration of 1.0 M as seen in Fig. 8. However, higher concentration results in more violent reaction. Hence, a number of bubbles being generated and agglomeration of these bubbles becomes more pronounced, leading to an even worse performance of the fuel cell at this situation. In addition, the flow pattern shown in both Fig. 6(j)–(l) and Fig. 8(j)–(l) at a volumetric flow rate of 1000 μL min^{-1} indicated that the mixing performance between two streams would be close to that without any addition of H_2O_2, as denoted as 0 M in Fig. 7(b), since there is almost no bubble presence in the microchannel.

Similar analysis was also made for two different kinds of membraneless microfluidic fuel cells that also produce carbon dioxide [7,12]. It is found in Fig. 9 that carbon dioxide produced in the electrochemical reaction can be completely dissolved into the liquid stream in the Choban's experiment whereas the carbon dioxide produced in the Jayashree's experiment is normally below the threshold value of solubility at their operating volumetric liquid flow rate, 0.3 mL min^{-1}. It is only at a current density above 110 mA cm^{-2}, as shown in Fig. 9, two-phase flow may be likely to occur. Such critical value is almost identical to the limiting value observed by Jayashree et al. [12]. Beyond this limiting current density, the authors suggested that crossover of formic acid to the cathodic stream would happen. In view of the foregoing discussions and flow visualization, it is therefore concluded that the influence of the gas/liquid two-phase flow on the performance of such membraneless microfluidic fuel cell may be quite crucial, and it is recommended that checking the threshold solubility with an operated flow rate is needed prior to conducting numerical simulation or experimental study for such membraneless microfluidic fuel cell.

4. Conclusions and suggestions

This study presents an analysis and a flow visualization experiment to examine the influence of two-phase flow on the fluid flow in membraneless microfluidic fuel cells. Prior the flow visualization experiment, an analysis is performed based on the comparison of the solubility of the gaseous product with the gas generation rate obtained by stoichiometry (Eqs. (5) and (6)) via their corresponding chemical equations.

The calculated results show that oxygen bubble is likely to be generated in Hasegawa's experiment [13] when the current density exceeds 30 mA cm^{-2} and 3 mA cm^{-2} for volumetric flow rates of 100 μL min^{-1} and 10 μL min^{-1}, respectively. Besides, it is found that the CO_2 bubble is also likely to be presented in the Jayashree's experiment [12] at current density above 110 mA cm^{-2} at their operating volumetric liquid flow rate, 0.3 mL min^{-1}. According to those calculation results, it is demonstrated that larger bubble in such microfluidic fuel cell would be easier to be formed either at the condition of higher current production or at a lower volumetric flow rate of the reactant.

For further clarification of this observation, a flow visualization using a 1000-μm-width and 50-μm-depth platinum-deposited Y-shaped microchannel is also conducted under laminar flow condition. Based on the flow visualization results, it is found that the presence of bubbles/slug is strongly connected with threshold solubility. When the operation is above the limit, two-phase flow prevails and the generated bubble/slugs can easily fill up the whole microchannel, thereby altering the flow field completely. Such bubble generation in the microchannel causes the mixing enhancement of the two inlet streams. Compared to the case without any H_2O_2 addition, the mixing index of the two inlet streams due to the effect of bubble generation in the microchannel is almost fivefold at the downstream when operated at a lower volumetric flow rate, 1 μL min^{-1}. By contrast, there are no detectable bubbles/slugs when the flow is being operated below the solubility limit. Hence, as the flow rate increases, 1000 μL min^{-1}, the mixing enhancement in the present study is insignificant due to no visible bubble formed in the microchannel. It is therefore concluded that the influence of the gas/liquid two-phase flow on the performance of such membraneless microfluidic fuel cell may be quite crucial.

A microfluidic membraneless fuel cells with high-aspect-ratio microchannel had been fabricated for observation of the bubble formation during the electric generation process. Measurements of the relevant polarization curve along with flow field visualization and related in-depth discussion of bubble effect on the performance of such microfluidic membraneless fuel cell is now being carried out. The gas bubble is indeed generated during the electric generation process. Both polarization measurement and flow fluid observation results will be presented in the near future.

Acknowledgement

The financial support provided to this study from the National Science Council of Taiwan under the Contract No. NSC 98-2221-E-151-056 is gratefully acknowledged.

References

[1] O. Savadogo, Emerging membranes for electrochemical systems. Part II: High temperature composite membranes for polymer electrolyte fuel cell (PEFC) applications. Journal of Power Sources 127 (2004) 135–161.

[2] T.V. Nguyen, R.E. White, A water and heat management model for proton-exchange-membrane fuel cells. Journal of the Electrochemical Society 140 (1993) 2178–2186.
[3] Y.M. Ferng, Y.C. Tzang, B.S. Pei, C.C. Sun, A. Su, Analytical and experimental investigations of a proton exchange membrane fuel cell. International Journal of Hydrogen Energy 29 (2004) 381–391.
[4] M.V. Williams, H.R. Kunz, J.M. Fenton, Operation of Nafion®-based PEM fuel cells with no external humidification: influence of operating conditions and gas diffusion layers, A parametric study of PEM fuel cell performances. Journal of Power Sources 135 (2004) 122–134.
[5] L. Wang, A. Husar, T. Zhou, H. Liu, A parametric study of PEM fuel cell performances. International Journal of Hydrogen Energy 28 (2008) 1263–1272.
[6] R. Ferrigno, A.D. Stroock, T.D. Clark, M. Mayer, G.M. Whitesides, Membraneless vanadium redox fuel cell using laminar flow. Journal of the American Chemical Society 124 (2002) 12930–12931.
[7] E.R. Choban, L.J. Markoski, A. Wieckowski, P.J.A. Kenis, Microfluidic fuel cell based on laminar flow. Journal of Power Sources 128 (2004) 54–60.
[8] E.R. Choban, J.S. Spendelow, L. Gancs, A. Wieckowski, P.J.A. Kenis, Membraneless laminar flow-based micro fuel cells operating in alkaline, acidic, and acidic/alkaline media. Electrochimica Acta 50 (2005) 5390–5398.
[9] E.R. Choban, P. Waszczuk, P.J.A. Kenis, Characterization of limiting factors in laminar flow-based membraneless microfuel cells. Electrochemical and Solid-State Letters 8 (2005) A348–A352.
[10] J.L. Cohen, D.A. Westly, A. Pechenikc, H.D. Abruña, Fabrication and preliminary testing of a planar membraneless microchannel fuel cell. Journal of Power Sources 139 (2005) 96–105.
[11] J.L. Cohen, D.J. Volpe, D.A. Westly, A. Pechenik, H.D. Abruña, A dual electrolyte H_2/O_2 planar membraneless microchannel fuel cell system with open circuit potentials in excess of 1.4 V. Langmuir 21 (2005) 3544–3550.
[12] R.S. Jayashree, L. Gancs, E.R. Choban, A. Primak, D. Natarajan, L.J. Markoski, P.J. A. Keni, Air-breathing laminar flow-based microfluidic fuel cell. Journal of the American Chemical Society 127 (2005) 16758–16759.
[13] S. Hasegawa, K. Shimotani, K. Kishi, H. Watanabe, Electricity generation from decomposition of hydrogen peroxide. Electrochemical and Solid-State Letters 8 (2005) A119–A121.
[14] M.H. Sun, G.V. Casquillas, S.S. Guo, J. Shin, H. Ji, O. Ouyang, Y. Chen, Characterization of microfluidic fuel cell based on multiple laminar flow. Microelectronic Engineering 84 (2007) 1182–1185.
[15] E. Kjeang, N. Djilali, D. Sinton, Microfluidic fuel cells: a review. Journal of Power Sources 186 (2009) 353–369.
[16] A. Bazylak, D. Sinton, N. Djilali, Improved fuel utilization in microfluidic fuel cells: a computational study. Journal of Power Sources 143 (2005) 57–66.
[17] F. Chen, M. Chang, C. Hsu, Analysis of membraneless microfuel cell using decomposition of hydrogen peroxide in a Y-shaped microchannel. Electrochimica Acta 52 (2007) 7270–7277.
[18] L.H. Lu, K.S. Ryu, C. Liu, A magnetic microstirrer and array for microfluidic mixing. Journal of Microelectromechanical Systems 11 (2002) 462–469.
[19] D.R. Lide, CRC Handbook of Chemistry and Physics. CRC Press, Boca Raton, 1992.
[20] M. Kawaji, P.M.Y. Chung, Adiabatic gas–liquid flow in microchannels. Microscale Thermophysical Engineering 8 (2004) 239–257.